

ROSAT spectro-imagery of the North Cygnus Loop

A. Decourchelle¹, J.L. Sauvageot¹, J. Ballet¹, and B. Aschenbach²

¹ Service d'Astrophysique, DAPNIA/DSM, CE-Saclay, F-91191 Gif-sur-Yvette Cedex, France

² Max-Planck-Institut für Extraterrestrische Physik, D-85740 Garching, Germany

Received 29 July 1996 / Accepted 20 January 1997

Abstract. We present a detailed analysis of the northern part of the Cygnus Loop using the spectro-imaging capability of the PSPC and the superior spatial resolution of the HRI on board the *ROSAT* satellite.

Large scale comparison between PSPC brightness and energy maps reveals that the bright emission structures are associated with soft emission, whereas the diffuse and faint regions correspond to harder one. Comparison with the optical image shows that the bright optical regions are associated with the soft and relatively bright X-ray emission, but not vice-versa. On the other hand, the hot tenuous X-ray regions do not show any optical emission. The interpretation of the north V-shaped structure in term of a bow-shock due to an interstellar cloud has been ruled out using the HRI, which shows filamentary emission along the western arm and diffuse emission with one bright knot on the eastern arm. Two close optical filaments underline the border of the shock front along the north rim as well as along the inner shell seen about 20 arcmin inside the remnant.

A detailed spectral analysis focussing on specific homogeneous regions is presented. In bright soft regions, a two component thermal model is needed. Both equilibrium and non-equilibrium ionization models reproduce well the spectra, but only the latter is consistent with the derived parameters. The lower temperature can explain most of the observed O VI emission. In faint hot X-ray region, a single non-equilibrium ionization model is possible, providing a lower column density than is usually accepted ($\simeq 10^{20} \text{ cm}^{-2}$). We investigate how neglecting the non-equilibrium ionization effects as well as the abundance variations can affect the spectral interpretation.

Key words: supernova remnants: Cygnus Loop – X-rays: ISM – ISM: Cygnus Loop

1. Introduction

Due to their large angular size, middle-aged supernova remnants constitute privileged targets for local studies, and among

them the Cygnus Loop is one of the best, at a distance of 300–800 parsec (Minkowski 1958, Braun and Strom 1986, Shull and Hippelein 1991, Greidanus and Strom 1992) and with a rather low absorbing column density (DeNoyer 1975). The Cygnus Loop supernova remnant has been mapped in X-rays by the *Einstein* IPC (Ku et al. 1984). Its X-ray image is fairly symmetric (circular within $\pm 5'$). The strong limb brightening and the presence of a hotter interior medium suggest an adiabatic Sedov model (Ku et al. 1984).

At smaller scales, some regions have been particularly affected either by the behaviour of the SN progenitor star (for example see Shull et al. 1985) or/and by the inhomogeneities in the interstellar medium as observed by the *Einstein* HRI and IPC (Ku et al. 1984, Charles et al. 1985) and by the *EXOSAT* CMA (Ballet and Rothenflug 1989) : "breakout" in the south, indentations of the X-ray shell, V-shaped structure in the north, etc. Much can be learned, studying in detail these irregularities, on the interaction of supernova remnants with the inhomogeneous ISM, and thus on the structure of the ISM in relation with clouds (Graham et al. 1995). On large scales, there is a rough correlation between the X-ray emission and the optical emission. It essentially concerns the east and the west limbs. In contrast, there is no bright optical counterpart to the X-ray bright northern shock front and to the bow-shock front in the southwest (Fig. 4a in Ku et al. 1984). We note that no bright X-ray emission is associated with the carrot-shaped optical filament, which covers a large part of the interior of the Cygnus Loop. A detailed comparison of the optical and X-ray emission has been carried out by Hester and Cox (1986) for a field in the south-eastern edge of the remnant, favouring a multiphase medium with large clouds ($R \geq 1 \text{ pc}$) immersed in a lower density "intercloud" medium.

Strong spectral variations have been observed over the Cygnus Loop by long IPC exposures (Charles et al. 1985), by the *TENMA* satellite (GSPC ; Tsunemi et al. 1988), by the *EXOSAT* satellite (CMA and ME ; Ballet and Rothenflug 1989) and suggest that the temperature distribution is bimodal ($\simeq 1.5 \cdot 10^6 \text{ K}$ and $\simeq 5 \cdot 10^6 \text{ K}$). High resolution spectroscopy with the *Einstein* FPCS (Vedder et al. 1986) shows emission lines from O VII, O VIII and Ne IX. The absence of any forbidden line emission

Send offprint requests to: A. Decourchelle
(decourchelle@sapvxa.saclay.cea.fr)

in the O VII triplet is evidence of out of ionization equilibrium conditions.

We will in the following concentrate on a part in the north of the Cygnus Loop. We have carried out observations of the north field with the *ROSAT* satellite (Trümper 1983, Aschenbach 1988), in order to study more deeply the V-shaped structure and associated spectra. The pointing was centred at $(\alpha, \delta)_{2000} = (20^{\text{h}}50^{\text{m}}02^{\text{s}}, +23^{\circ}11'23'')$. The exposure time was of 3,337 seconds with the Position Sensitive Proportional Counter (PSPC; Pfeffermann et al. 1986). Observations were also performed using the High Resolution Imager (HRI) with an exposure time of 16,000 seconds. The PSPC pointing was obtained from April 25 to May 5, 1991 and the HRI pointing from November 6, 1991 to May 22, 1992.

The paper is organized as follows : Sect. 2 is dedicated to the morphological study of the north field using PSPC and HRI data, and a comparison with optical images. Sect. 3 focuses on a detailed spectral study of specific regions. In Sect. 4, we discuss and interpret the results. The conclusions are presented in Sect. 5.

2. X-ray morphology of the north field

2.1. The PSPC image of the north Cygnus Loop

The PSPC image is shown in Fig. 1a and confirms the *EXOSAT* features (Ballet and Rothenflug 1989) : the large surface brightness contrast between the eastern and the western sections, and the bright V-shaped structure. The shock front north of this structure shows steeper brightness profile than in the neighbourhood (see contours in Fig. 1b), which suggests a higher ambient density especially in comparison with the western half, which exhibits a small bubble-like extension and less organized X-ray contours. On the eastern half, we observe a double shell structure in a direction parallel to the shock front. In the inner part of the remnant, the emission is faint and diffuse with small density variations.

The optical image is superposed on X-ray contours in Fig. 2a, which reveals a clear but not systematic correlation. The bright optical regions correspond to soft (see the energy image, Fig. 1b) and relatively bright X-ray emission, but not vice versa. All the bright and soft X-ray regions do not show bright optical counterparts, as seen in the brightest blob (Field A) of the PSPC observation. Even in case of a clear correlation, we note that the morphologies are different. In the "carrot" area, the optical emission is much more enhanced than in X-rays, with a larger extent and slight shift toward the west. A contrary behaviour is observed for the V-shaped structure, which shows strong extended X-ray emission with optical emission limited along a preferential axis (along the west arm and its extension). In the hot and tenuous X-ray regions (yellow patches in the energy image, Fig. 1b), no optical emission is visible.

Two close faint filaments mark the position of the X-ray shock front (Figs. 2a and 2b). They are likely to be the extension of the two north-east Balmer-dominated filaments studied by Hester et al. (1986) and Hester et al. (1994). Such nonra-

diative shocks have been observed in a number of supernova remnants (Kulkarni and Hester 1988, Raymond 1991) to mark the location of the blast wave. They are attributed to the presence of neutral hydrogen atoms in the ambient medium, which are suddenly heated by the blast wave leading to collisional excitation, ionization and charge transfer.

On the eastern half of the PSPC pointing, a double shell structure appears which is distinct in surface brightness map (see regions P1,P2,P3,P4 on Fig. 1a) and in energy map (Fig. 1b). This very regular double shell structure is also present in optical with a separation of about 20 arcmin ($\simeq 5$ pc at a distance of 770 pc). This feature starts in the north-east and extends in the west side of the Cygnus Loop as can be seen on the red POSS image (see Fig. 4 in Hester 1987). Through the west arm of the X-ray V-shaped structure and the optical "carrot" complex, this structure might be masked by the brighter emission. The inner shell is present in a region lacking strong optical filaments (i.e. no strong interaction with clouds). The two shells (inner and outer) join when encountering clouds like in the eastern and western parts as can be seen in the *ROSAT* all-sky survey image of the Cygnus Loop (Aschenbach 1992). Optical spectroscopy of the thin inner filamentary structure should provide some clues to the origin of these features.

2.2. HRI observation of the V-shaped structure

The IPC composite image (Ku et al. 1984) indicates a V-shaped structure in the northern area of the Cygnus Loop, but due to a missing field in the cartography, further analysis could not be carried out. The CMA images (Ballet and Rothenflug 1989) of the north field exhibit a bright huge V-shaped (or X-shaped) structure, which extends far into the remnant (in projection), and surrounding a faint zone. But the statistics in the CMA image was not sufficient to resolve properly the morphology. As discussed by Ballet and Rothenflug (1989), it might be reminiscent of a bow shock, associated with the interaction of the remnant with a dense cloud, but in this case the maximum of the emission would be expected at the tip of the structure, where the hot gas is more compressed contrary to what is observed (see figure 4b in Ballet and Rothenflug 1989). The brightest X-ray emission is located on the east side ($(\alpha, \delta)_{2000} = 20^{\text{h}}48^{\text{m}}20^{\text{s}}, 31^{\circ}58'$). The high resolution image of the *ROSAT* HRI is used to focus more specifically on this V-shaped structure (Figs. 3 and 4, see also the colour picture in Sauvageot and Decourchelle 1995).

The superposition of the HRI surface brightness contours on the optical POSS image is shown on Fig. 3. No strong optical emission is associated with the north X-ray structure. However, a detailed comparison between the X-ray brightness (at the resolution of the HRI) and the optical filaments reveals a good correlation along the west arm down to the south-east extension of the V-shaped structure. The X-ray filament is associated with the faint optical filaments all along the western arm, while at the tip of the structure, the diffuse X-ray emission is associated with diffuse optical emission. Conversely, no such correlation is apparent along the eastern arm, except of a small faint filament which begins nearby the bright condensation and ends in the

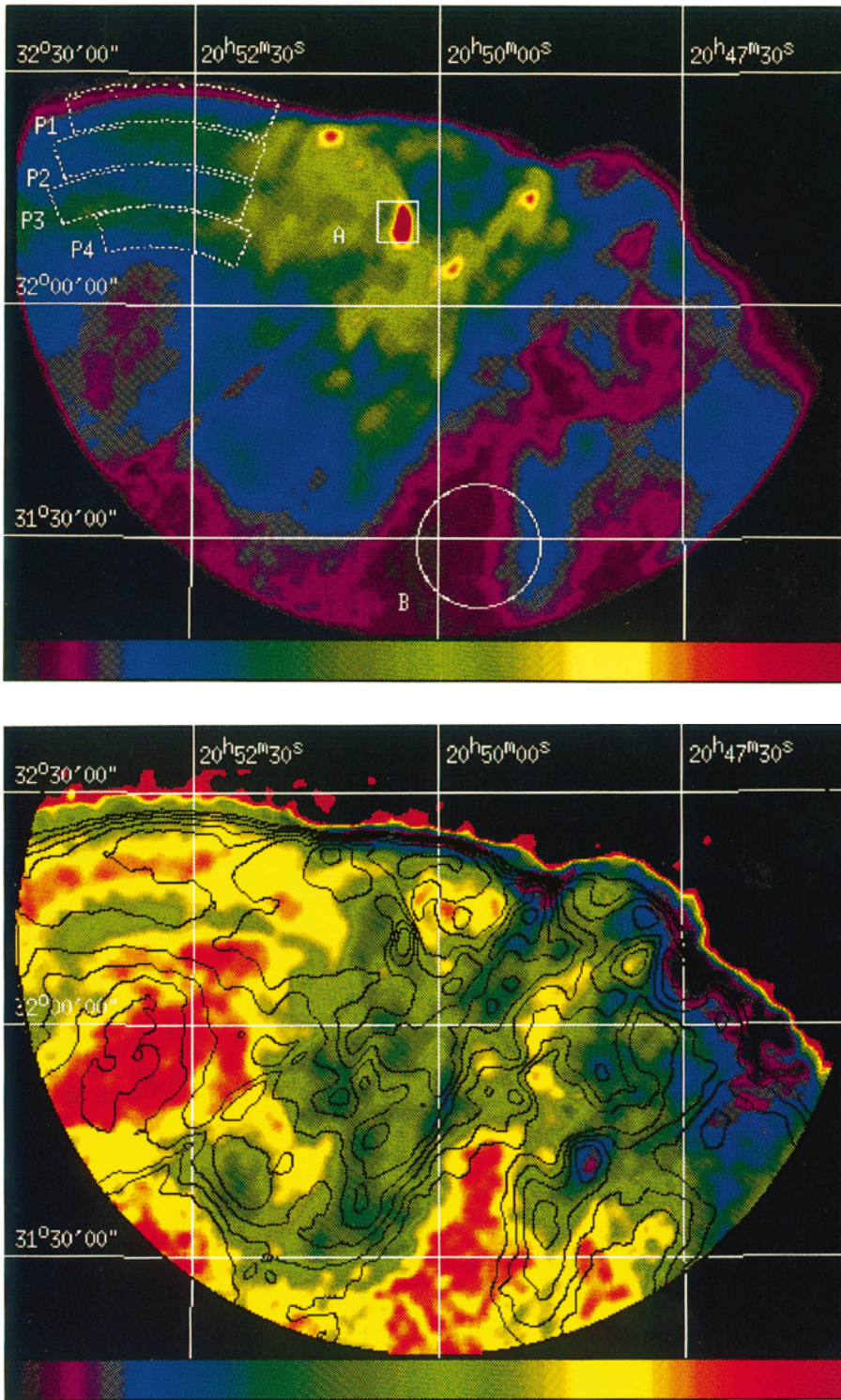


Fig. 1. **a** *ROSAT* PSPC image of the north Cygnus Loop, smoothed with a two-dimensional gaussian of $\sigma = 45$ arcsec. **b** Smoothed *ROSAT* PSPC energy image (see Sect. 3) on which are superposed the brightness contours. The contour levels are logarithmically spaced (by 0.13 digits) with the lowest contour at 10^{-5} counts/s/arcsec². The outer ring contaminated by high energy particles has been excluded from these images. The smearing at the shock front in the energy image is an effect of the gaussian filtering. The fluctuations seen at the border and outside the remnant are artificial, due to the method of creating the smoothed energy image, which is not valid for the low count levels of the background.

faint X-ray region between the two arms. But it is not clear if the filament is physically associated with this blob or not. The brightest X-ray region corresponds to a denser medium (cloud), in which radiative shocks are expected. The absence of clear optical emission suggests that the bright knot had no time to undergo radiative shocks, due either to a recent shock or to a low knot density.

There is a good correlation with the other spectral bands. The V-shaped structure is observed at radio wavelengths (Green 1984) and in the ultraviolet (O VI line ; Blair et al. 1991). The good correlation between the IR and the X-ray images of the Cygnus Loop is well known at large scale (Braun and Strom 1986, Arendt et al. 1992). The correlation is excellent at smaller scales between the IRAS 60 microns brightness and the HRI

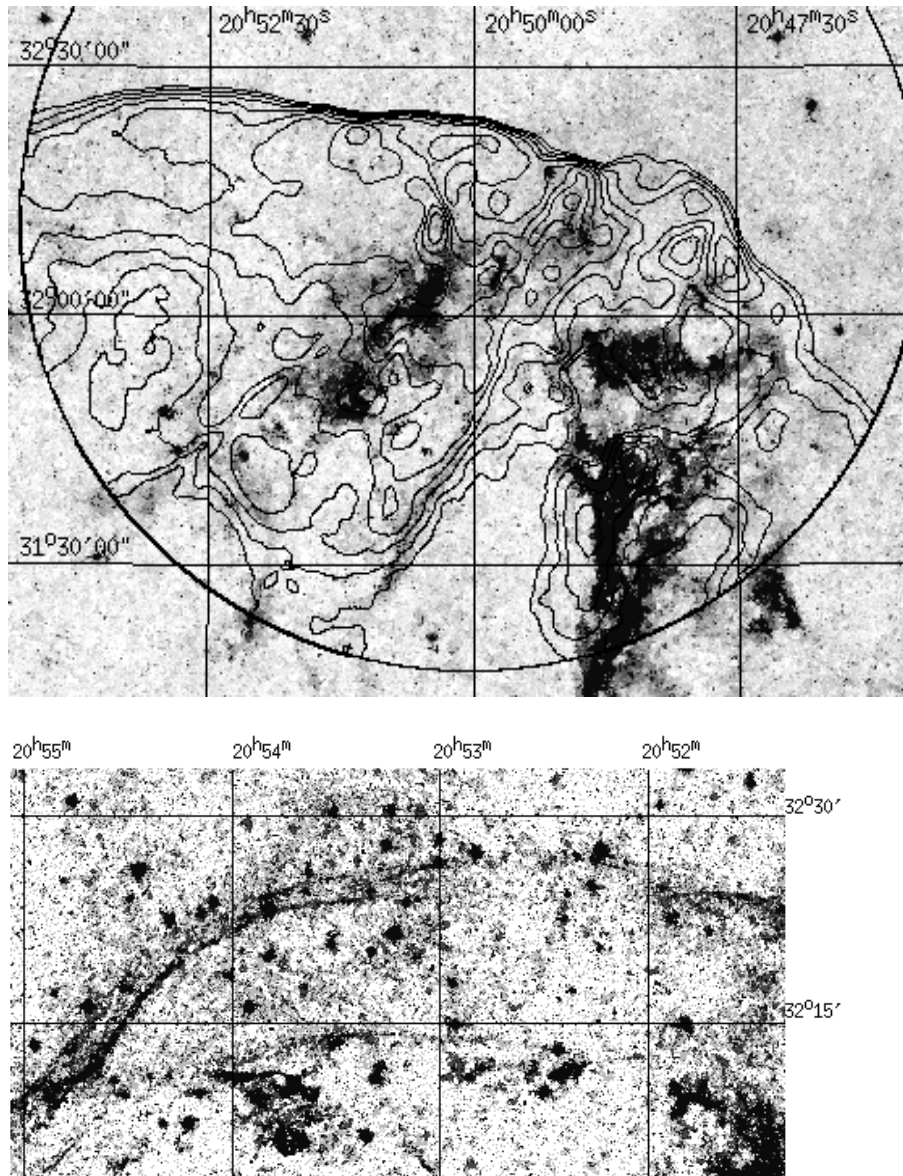


Fig. 2. **a** Optical POSS image of the north Cygnus Loop overlaid with PSPC X-ray logarithmic contours (same as Fig. 1b). **b** Optical POSS image of the double shell structure along the north Cygnus Loop shock front.

brightness (as shown in Fig. 4), indicating that the emission process is mainly due, in this region, to the heating of interstellar grains by hot electrons of the plasma.

The small scale structures no longer favour a bow shock model : the western arm appears as a rather "filamentary" structure (in X-rays and in the optical band), and seems to run to the south-east extension, whereas the eastern arm presents more diffuse emission, with one bright knot. We note that the X-ray shell presents indentations at the end of each arm (east and west). The two arms appear to be independent and the V-shaped structure may simply be due to a projection effect. Velocity measurements of the hot gas, obtained by Fabry-Pérot observations of iron coronal lines (Sauvageot and Decourchelle 1995), confirm this result : the eastern arm is on the rear side (going away from us) whereas the western arm is on the near side (moving toward us). This is in agreement with the presence of clouds in front of

the north-west half of the remnant, as observed in HI (DeNoyer 1975) and in the infrared (Braun and Strom 1986).

3. Spectral analysis of specific areas

In order to investigate the large scale spectral variations, we create a smoothed energy map. A so-called power image is computed by summing the energies of the photon per pixel. This image is convolved by a Gaussian of $\sigma = 105$ arcsec. We apply the same filter on the brightness image and then obtain a smoothed energy image by dividing the convolved power image by the convolved brightness image. This smoothed energy map (Fig. 1b) exhibits large and small scales inhomogeneities, which are generally anticorrelated with the brightness image: the bright structures exhibit a soft spectrum, whereas the faint and diffuse emission regions have a harder spectrum. This indicates that the pressure equilibrium is grossly maintained. The

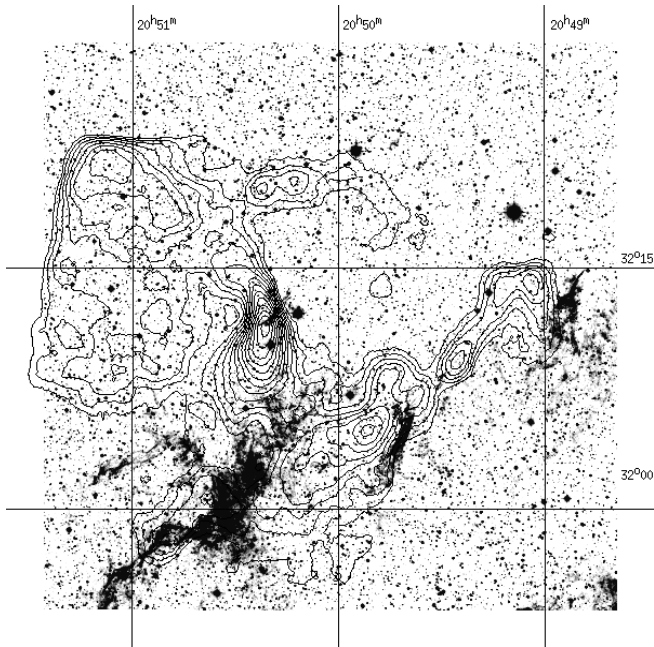


Fig. 3. Smoothed logarithm HRI X-ray contours overlaid onto the optical POSS image of the V-shaped structure. A Gaussian smoothing has been applied on the HRI image with $\sigma = 24$ arcsec. The contour levels are logarithmically spaced (by 0.045 digits with the lowest contour at 0.125 counts/arcsec²).

soft component is prominent in the limb and particularly along the V-shaped structure and its sharp shock front, indicating an interaction with a denser medium. The inner volume is filled with a hot and tenuous gas. Studying the spectral differences should allow us to understand more deeply the interaction of the Cygnus Loop with its environment.

In order to obtain further spectral informations on the V-shaped structure, we superpose the X-ray contours in the band 0.1-0.2 keV on the brightness image in the band 0.8-2.4 keV, as shown in Fig. 5. At higher energies, the north-west blob has completely disappeared, as well as the emission at the top of the east arm. The brightest X-ray blob is still emitting above 0.8 keV as well as the inner structures. This suggests that the bright blobs at the shock front have just been engulfed by the blast wave, explaining their low temperature and absence of optical emission, whereas the inner emission regions show higher temperatures and generally more optical emission. But projection effects prevent us to conclude whether the inner blobs are actually close to the shock front.

The emitting conditions vary from place to place and simple models cannot account for the spectrum of the whole field. We thus select small regions as homogeneous as possible (in energy and brightness) in order to determine the main components of the spectra. We will focus on a detailed analysis of two regions (Fields A and B, see Fig. 1a), which exhibit very different spectral and morphological characteristics. We choose the brightest knot of our pointings located on the east arm, which presents a very soft spectrum. On the other hand, the faint inte-

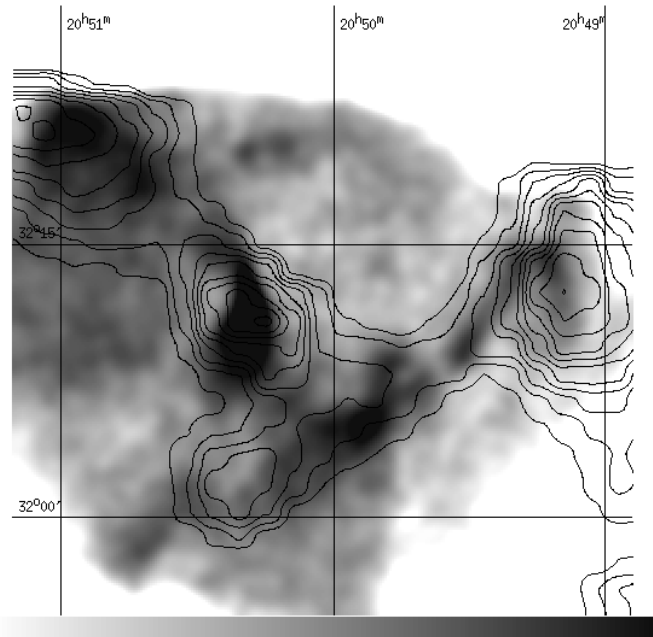


Fig. 4. *ROSAT*HRI image (smoothed as Fig.3) of the V-shaped structure overlaid by the IRAS 60 micron contours. The grey scale is logarithmic. The IRAS image was smoothed by a 2-D Gaussian with a $\sigma = 270$ arcsec. The contour levels are spaced by 0.2 mJ/steradian with the lowest contour at 4.5 mJ/steradian.

rior gas (Field B) exhibits a harder spectrum. The spectral fitting is done with thermal models using the ionization and recombination rates from Arnaud and Rothenflug (1985) and Arnaud and Raymond (1992) and the emission model of Mewe et al. (1985, 1986). We assume solar abundances taken from Meyer (1985). For non-equilibrium ionization (NEI) models, we compute directly the spectra instead of interpolating in a precomputed grid. The code is thus more resistant to local minima and the convergence is much improved. Due to a better determination of the emissivities and the derived best parameters, the error bars are much more reliable.

3.1. Collisional ionization equilibrium

A general feature of the spectra, both of Field A and Field B, is that a model with a single temperature plasma in collisional ionization equilibrium does not reproduce the shape of the spectra above 1 keV. Table 1 and Table 2 summarize the best fit parameters for all applied models and extracted spectra. In this paper, we assume a distance D to the Cygnus Loop of 770 pc (Minkowski 1958).

In all homogeneous regions, a very good fit is achieved with a two temperature model. In Field A, the emission measure EM_1 of the low component ($kT_1 \simeq 0.1$ keV) dominates largely that (EM_2) of the hot component ($kT_2 \simeq 0.3$ keV). The ratio EM_1/EM_2 shows strong variations (from $\simeq 5$ to 20) within our pointings. The two components of the B field are hotter than those of the A field. The hydrogen column density N_H in

Table 1. Spectral models for Field A, X-ray softest region.

Models	kT_1 keV	EM_1 $\text{cm}^{-6} \text{ pc}$	$\log(n_{et})_1$ s cm^{-3}	kT_2 keV	EM_2 $\text{cm}^{-6} \text{ pc}$	$\log(n_{et})_2$ s cm^{-3}	N_H cm^{-2}	$^* \chi_r^2$
EI	0.17	9	-	-	-	-	$1.6 \cdot 10^{20}$	4.
NEI	0.34	2	10.4	-	-	-	$0.9 \cdot 10^{20}$	2.
2 EI	0.12 ± 0.01	35 ± 18	-	0.29 ± 0.03	1.6 ± 0.4	-	$4.5 \pm 1 \cdot 10^{20}$	0.9
EI + NEI	0.065 ± 0.025	180^{+7000}_{-140}	-	0.5 ± 0.1	$1.2^{+0.9}_{-0.5}$	$10.15^{+0.3}_{-0.15}$	$6.^{+3}_{-1.5} \cdot 10^{20}$	0.9
2 NEI : Sol. 1	$0.12^{+0.02}_{-0.07}$	$35^{+5300**}_{-18}$	$9.7 [\geq 9.3]$	$0.3^{+0.06}_{-0.02}$	$2.0^{+1.1}_{-1.2}$	$13 [\geq 11]$	$6.^{+2.4}_{-2.5} \cdot 10^{20}$	0.9
2 NEI : Sol. 2	$0.065^{+0.08}_{-0.06}$	$120^{+5300**}_{-18}$	$13 [\geq 9.3]$	0.5 ± 0.1	$1.2^{+1.8}_{-0.5}$	$10.15^{+0.35}_{-0.15}$	$6. \pm 2.5 \cdot 10^{20}$	0.9

* χ_r^2 is the reduced chi-squared value. The error bars are for the 90 % confidence level.

** These large error bars correspond to a low temperature and high N_H , to which the PSPC becomes insensitive.

Table 2. Spectral models for Field B, X-ray hot region.

Models	kT_1 keV	EM_1 $\text{cm}^{-6} \text{ pc}$	$\log(n_{et})_1$ s cm^{-3}	kT_2 keV	EM_2 $\text{cm}^{-6} \text{ pc}$	$\log(n_{et})_2$ s cm^{-3}	N_H cm^{-2}	$^* \chi_r^2$
1 EI	0.2	0.7	-	-	-	-	$1.7 \cdot 10^{20}$	2.3
1 NEI	$0.7^{+0.2}_{-0.1}$	$0.1^{+0.02}_{-0.01}$	10.15 ± 0.15	-	-	-	$1 \pm 0.2 \cdot 10^{20}$	1.2
2 EI	0.2 ± 0.1	1.2 ± 0.2	-	0.56 ± 0.1	0.2 ± 0.02	-	$2.7 \pm 0.3 \cdot 10^{20}$	1.2
EI + NEI	$0.035 [\leq 0.08]$	$740 [\geq 1]$	-	0.5 ± 0.1	$0.2 [\geq 0.1]$	10.25 ± 0.15	$9^{+3}_{-5} \cdot 10^{20}$	1.2

* χ_r^2 is the reduced chi-squared value. The error bars are for the 90 % confidence level.

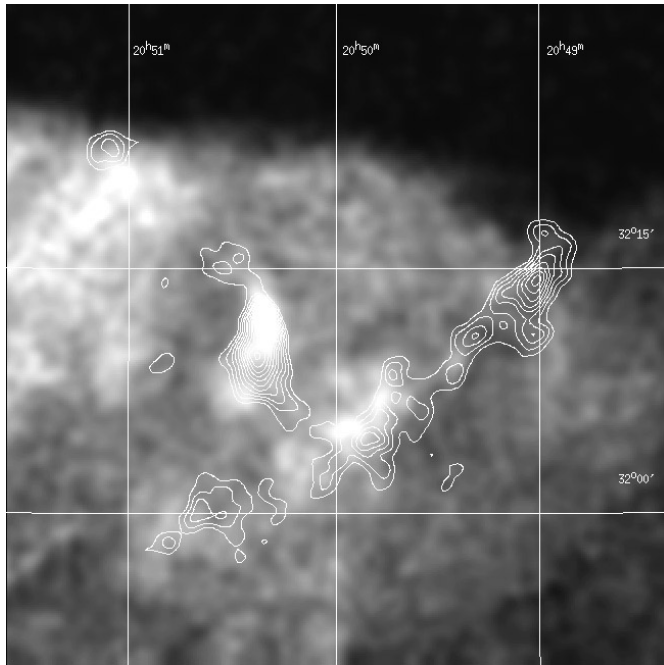


Fig. 5. PSPC X-ray contours of the V-shaped structure in the band 0.1-0.2 keV superimposed on the brightness image in the band 0.8-2.4 keV. Both images were smoothed by a $\sigma = 45$ arcsec Gaussian. Contour levels are spaced by 10^{-3} counts/arcsec² with the lowest contour at $9 \cdot 10^{-3}$ counts/arcsec².

Field B is 2 times lower than in Field A, which is in agreement with the value ($\simeq 4 \cdot 10^{20} \text{ cm}^{-2}$) derived from previous X-ray data (Ku et al. 1984). This N_H variation is consistent with the

HI measurements at 21 cm toward this region of the Cygnus Loop (DeNoyer 1975). These HI observations, however, indicate a larger column density of $7 - 15 \cdot 10^{20} \text{ cm}^{-2}$.

Despite the result that the fits are formally acceptable, the plasma is not expected in collisional ionization equilibrium (CIE), particularly not the hot tenuous gas which has a low density. The soft component is denser but, on the other hand, should have been shocked more recently. Both components may thus exhibit out of equilibrium ionization, depending more precisely on the densities and the time elapsed since the gas has been shocked which we will investigate in the following.

We can estimate the expected ionization parameter n_{et} , assuming the distance D and an approximate volume of the emitting gas. Given the fact that the soft X-ray emission is strongly correlated with the bright emission structures, we conclude that these regions include density enhancements (clouds) and we assume this component to be locally confined. In contrast, the hot component arises from the whole volume of the SNR. The size of Field A is $315'' \times 315''$. We approximate the emitting region of the soft component by a cube of 1.2 pc length, and the region of the hot component by a parallelepiped of about 22 pc depth. For field A, the derived mean densities are $n_1 \simeq 5.5 \text{ cm}^{-3}$ and $n_2 \simeq 0.15 \text{ cm}^{-3}$. This gives a mass of about $5 \cdot 10^{-2} M_\odot$ for the bright blob. If we take t , the time elapsed since the gas has been shocked, to be 18000 yr, which is an upper limit corresponding to the age estimated for the Cygnus Loop (Ku et al. 1984), it leads to $(n_{et})_1 \simeq 3 \cdot 10^{12} \text{ s cm}^{-3}$ and $(n_{et})_2 \simeq 9 \cdot 10^{10} \text{ s cm}^{-3}$. The region B is located more in the interior of the remnant (in projection) and shows no particular emission structure that could be linked to the soft component. We thus assume a filling factor of the soft component around 10% and a

cylinder of 34 pc depth and a radius of 2 pc (Field B is a circular region of radius 472.5 arcsec). We derive mean densities ($n_1 \simeq 0.6 \text{ cm}^{-3}$, $n_2 \simeq 0.07 \text{ cm}^{-3}$) and mean ionization parameters ($(n_e t)_1 \simeq 3. \cdot 10^{11} \text{ s cm}^{-3}$, $(n_e t)_2 \simeq 4. \cdot 10^{10} \text{ s cm}^{-3}$), demonstrating that the plasma is not in ionization equilibrium, which is the case only for $n_e t$ close to (and higher) than $10^{12} \text{ s cm}^{-3}$ (as estimated from the relevant ionization rate, Arnaud and Rothenflug 1985).

3.2. Non-equilibrium ionization

Evidence of NEI in the Cygnus Loop has been obtained by Vedder et al. (1986) from the *Einstein* FCPS data on the north field of the Cygnus Loop. The excellent spectral resolution has allowed a very good NEI diagnostic from the O VII and O VIII lines, but the narrow energy band was insufficient to characterise the whole spectrum. The spectral resolution of the instruments which have followed was insufficient to discriminate between CIE and NEI models (Tsunemi et al. 1988, Ballet and Rothenflug 1989). Recently, *ASCA* SIS observations have confirmed NEI conditions of the plasma in the north-east (Miyata et al. 1994) and north of the Cygnus Loop (Miyata et al. 1995). We stress that the existence of NEI conditions cannot be demonstrated with the PSPC because of its limited spectral resolution, and both EI and NEI models provide acceptable fits. But within the framework of NEI models, we can derive the ionization parameters including $n_e t$ and check for NEI model consistency between the soft (cool) and hot components taking into account their spatial distribution.

3.2.1. A single NEI component

For field A, the fit with a single NEI model is poor with $\chi^2 \simeq 2$ as shown in Fig. 6a. The best fit temperature is high, similar to the hot component of the 2T equilibrium model and the ionization parameter is small (Table 1). We note a low hydrogen column density ($N_H \simeq 0.9 \cdot 10^{20} \text{ cm}^{-2}$). The analysis shows that the model predicts emission too low above 1 keV due to a lower continuum and a lower ionization state of magnesium and silicon, compared to the two temperature equilibrium model. Furthermore, the NEI emission is too high around 0.5-0.7 keV (O VII and O VIII lines) and too low around 0.3-0.4 keV (C V et C VI lines). Clearly, a single NEI model cannot account for the soft spectrum of Field A.

However, we expect the spectrum of the faint and hot regions to be consistent with a single NEI model, since they show no morphological signatures of the soft component. They should thus correspond to the shocked interstellar medium (ISM). In fact, these regions are compatible with a single $n_e t$ component with a hot temperature (Fig. 6b). In Field B, the temperature is 0.7 keV and the ionization parameter $\simeq 1.4 \cdot 10^{10} \text{ s cm}^{-3}$. We estimate the average density to be 0.06 cm^{-3} and an ionization age of 7000 years. We study another faint diffuse region (Field C centered at $(\alpha, \delta)_{2000} = (20^{\text{h}} 52^{\text{m}} 54^{\text{s}}, +31^{\circ} 54' 54'')$) located closer to the shock front (compared to the Field B) and derived a density around 0.1 cm^{-3} and an ionization age of 4000 years.

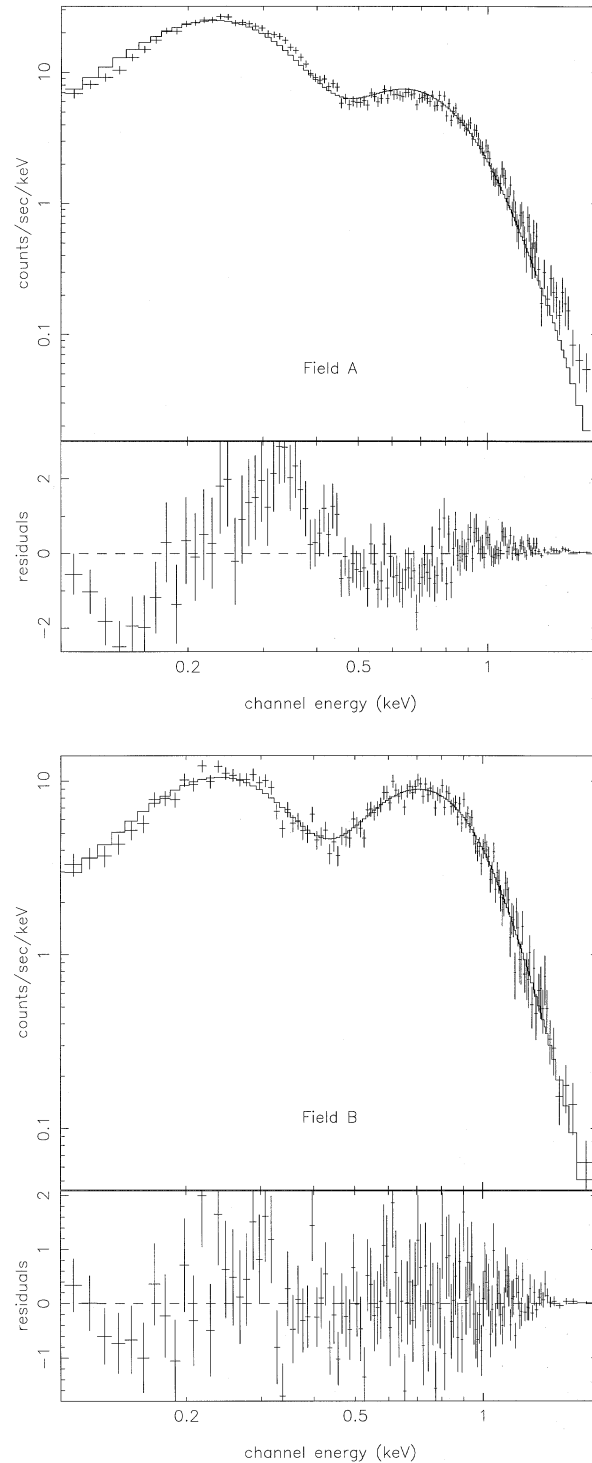


Fig. 6. **a** Fit of the Field A spectrum with a single NEI model. **b** Fit of the Field B spectrum with a single NEI model.

This is reasonable in view of the outlying position of the two fields : in the center, we expect the density to be lower and the ionization age larger. However, within the error bars, we do not observe a clear increase of the temperature in the center (0.8 keV instead of 0.7 keV). This model requires a rather low value of N_H ($\simeq 10^{20} \text{ cm}^{-2}$) to fit the data.

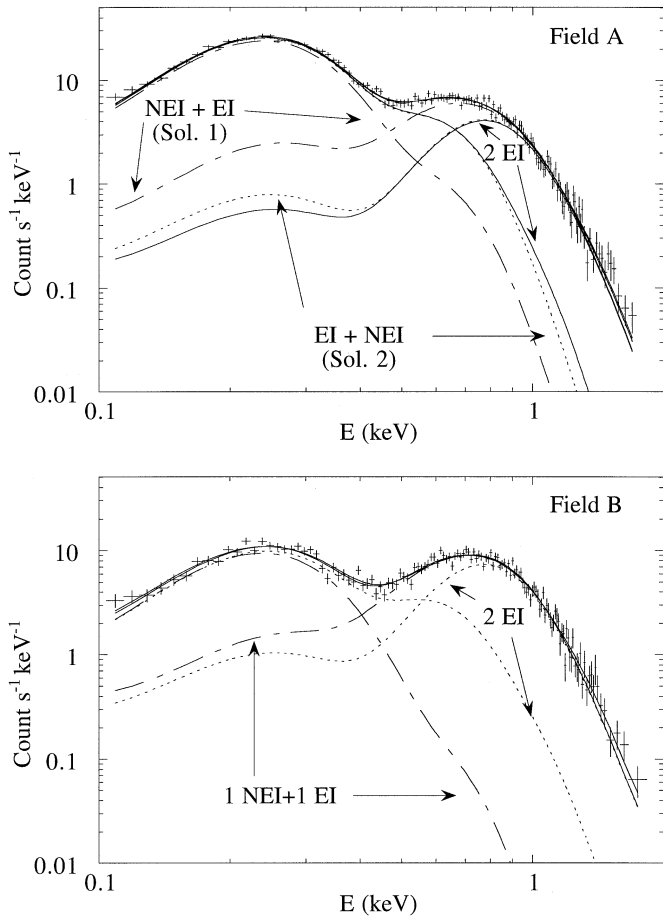


Fig. 7. **a** Comparison for Field A of the soft and hot components for the best fit models. **b** Comparison for Field B of the contribution of the soft and hot components for two component models.

3.2.2. Model with one EI component and one NEI component

In a first step, we add an EI component to model the soft component of the Field A spectrum and to compensate for the low value of N_{H} of Field B. The fit (Fig. 7) is as good as with two EI components (Tables 1 and 2) and good constraints on the parameters are derived for Field A.

For the hot Field B (Fig. 7b), the constraints on the soft component are poor. An upper limit of the low temperature has been derived (Table 2), but no lower limit could be set basically because of the reduced sensitivity of the PSPC below 0.1 keV. As a consequence, upper limits on the emission measures cannot be derived. The best fit parameters of the soft component are unrealistic, as the very high value of the emission measure ($740 \text{ cm}^{-6} \text{ pc}$) shows. But, the interesting point is that assuming a soft component with $kT \simeq 0.06\text{--}0.08 \text{ keV}$ (acceptable at the 90% confidence level), we obtain a reasonable emission measure (a few $\text{cm}^{-6} \text{ pc}$) and a higher N_{H} ($\simeq 5.10^{20} \text{ cm}^{-2}$). The low N_{H} obtained in the one component NEI model can be brought back to a more usual value invoking a low temperature EI component.

We derive the averaged densities in Field A ($n_1 \simeq 6 \text{ cm}^{-3}$, $n_2 \simeq 0.14 \text{ cm}^{-3}$) and Field B ($n_1 \simeq 0.7 \text{ cm}^{-3}$, $n_2 \simeq 0.08 \text{ cm}^{-3}$). We chose a filling factor of 10% for the soft component in Field B. This value is probably too large and underestimates the density. The value of the ionization parameter is high ($n_e t \simeq 1.5 \cdot 10^{10} \text{ s cm}^{-3}$) and we derive an age of 3000 yr for Field A and 7000 yr for Field B. The dependence on temperature, density and ionization time is qualitatively similar to a Sedov model.

3.2.3. Model with two NEI components

As is estimated in 3.1, NEI effects are also expected for the soft component, which should have been shocked later. We thus investigate whether the spectrum of Field A can be modelled with two NEI components (Table 1). Fig. 7a shows the best fit models and the contributions of each component. We find in the chi-squared distribution two minima, which correspond to the low component in a non-equilibrium state, associated with a hot component in equilibrium, and the opposite configuration for the second minimum (see Sol. 1 and Sol. 2 in Table 1). This indicates that the soft and hot components cannot be explained by strong NEI effects simultaneously. The upper value of $n_e t$ is not constrained for the soft component (≥ 9.3) and is thus compatible with ionization equilibrium state, whereas the hot component (Sol. 2) is significantly in a NEI state (at 90% confidence level, but not at 99%). The second solution recovers the results of the previous (EI+NEI) model, to which we refer for the derived parameters. For solution 1, we obtain a density of $\simeq 6 \text{ cm}^{-3}$ and an age of about 50 years. This gives a very young age for the bright knot. However, the uncertainties are much larger for NEI models, due to the lack of constraints.

3.3. Variations of elemental abundances

The importance of elemental depletion in SNRs X-ray spectra was first pointed out by Itoh (1989), and more recently by Vancura et al. (1994). The energy resolution of the PSPC does not allow to constrain the element abundances, so they were assumed to be solar for all the previous fits. However, in this section, we investigate whether abundances different from solar can improve the spectral fits. For example, a single NEI model cannot reproduce the Field A spectrum: the brightness predicted is too low above 1 keV and around 0.3-0.4 keV, and too high at 0.5-0.7 keV. A good fit ($\chi^2 \simeq 0.9$) is obtained with an underabundance of $0.5 \pm 0.1 \text{ Ab}_{\odot}$ for oxygen. This value is very low compared with the fraction of oxygen in the ISM depleted from the gas phase (20 % bound into interstellar grains, see Itoh 1989 and Savage and Mathis 1979). Note that even stronger oxygen underabundances ($0.036 \pm 0.002 \text{ Ab}_{\odot}$ in the north-east and $0.073 \pm 0.003 \text{ Ab}_{\odot}$ in the north) have been derived from the ASCA observations of the Cygnus Loop (Miyata et al. 1994, Miyata et al. 1995). This oxygen abundance problem may arise from the uncertainties on the emissivities used for the iron L complex.

Table 3. X-ray predicted O VI line emission.

Fields	Model	Predicted surface brightness erg cm ⁻² s ⁻¹ sr ⁻¹
Field A	2 EI	4 10 ⁻⁶
	EI + NEI	59 10 ⁻⁶
	2 NEI sol. 1	3 10 ⁻⁶
	2 NEI sol. 2	41 10 ⁻⁶
Field B	2 EI	0.05 10 ⁻⁶
	EI + NEI	0.2 10 ⁻⁶

3.4. Expected O VI line emission

Blair et al. (1991) have obtained an O VI emission map at 1035 Å of the Cygnus Loop with the *Voyager 2* ultraviolet spectrometer. The O VI emission is widespread throughout the remnant and is well correlated with the soft X-ray image. The average observed surface brightness Σ is $8.8 \cdot 10^{-6}$ erg cm⁻² s⁻¹ sr⁻¹ and the peak surface brightness observed is $26 \cdot 10^{-6}$ erg cm⁻² s⁻¹ sr⁻¹. Field A is within the brightest regions and thus its O VI surface brightness should be comparable to the observed peak surface brightness. But due to the large *Voyager 2* field of view ($0.1^\circ \times 0.87^\circ$), this value only provides some reasonable estimate. Field B corresponds to the faintest regions and the average observed surface brightness is thus not representative.

In this section, we estimate the amount of O VI emission which can be produced by the soft X-ray plasma. Using the parameters derived from the fit to the *ROSAT* data ($T, n_{e,t}, EM, N_H$), we determine the O VI emission for each model and each field and we compare it to the measurements.

The O VI surface brightness can be written as :

$$\Sigma = \frac{EM}{4\pi} \frac{P}{n_e^2} = \frac{EM}{4\pi} \mathcal{E}(T) X_5(T, n_{e,t}) \frac{[O]}{[H]}$$

where EM is the emission measure, P the power per unit volume, n_e the electronic density, $\mathcal{E}(T)$ the line emissivity of the O VI doublet (Raymond and Smith 1996), $X_5(T, n_{e,t})$ the O⁵⁺ ionic fraction and $[O]/[H]$ the oxygen abundance. We use the ionization and recombination rates from Arnaud and Rothenflug (1985) and the abundance from Meyer (1985).

We use the value of N_H derived from the *ROSAT* fit to correct for the ultraviolet absorption at 1035 Å. The reddened O VI line surface brightness Σ_{red} is :

$$\Sigma_{red} = 10^{-A_\lambda/2.5} \Sigma$$

where $A_\lambda = (16.17 - 3.20 \frac{1}{\lambda} + 0.297 \frac{1}{\lambda^2}) E_{B-V}$ (Seaton 1979)

$$\text{and } E_{B-V} = \frac{N_H \text{ cm}^{-2}}{7.5 \cdot 10^{21}} \text{ mag} \quad (\text{Jenkins and Savage 1974})$$

The O VI emission derived from the soft X-ray gas is summarized in Table 3. Strong emission is expected in Field A (soft X-ray spectrum), whereas very little emission is expected in the hot Field B. This is qualitatively in agreement with the

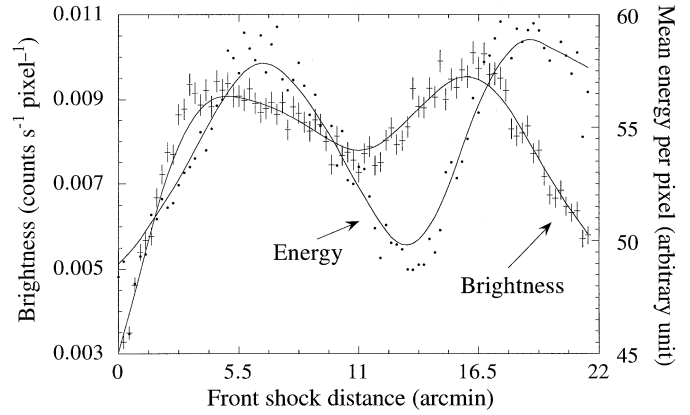


Fig. 8. Profiles of the mean energy per photon and brightness across the double shell structure from the shock front. The lines represent the profiles derived from the smoothed images (convolved with a Gaussian of $\sigma = 105$ arcsec), whereas the points, with a larger scattering, are from the raw images. We note that the photon flux and energy peaks are clearly shifted.

O VI emission map from Blair et al. (1991). For Field A, 2 EI and 2 NEI (sol. 1) models produce less than half of the average observed value, while (EI + NEI) and 2 NEI (sol. 2) produce roughly twice the peak observed value.

The excellent correlation between the O VI and soft X-ray maps (Blair et al. 1991) indicates that the O VI emission is related to the soft X-ray plasma. It seems that the O VI emission is likely to be almost entirely produced by the soft component of the X-ray plasma, assuming that the soft component is in equilibrium while the hot component is out of equilibrium. But only future spatially resolved spectroscopy in the ultraviolet can assess the relative contributions of O VI emission from the X-ray emitting plasma and radiative shocks (bright optical regions).

3.5. The double shell structure

A general feature in the *ROSAT* PSPC observation of the North field is the anticorrelation between the brightness and the energy images, indicating that the pressure is roughly conserved. Even if this is a general tendency, we may still expect some pressure variation in specific places. As discussed in Sect. 2.1, the double shell structure is of particular interest. A close view of the brightness and energy profiles (Fig. 8) shows that they are slightly but clearly shifted, which indicates a striking pressure behaviour. We can invoke some mechanisms like NEI effects at the shock front to explain it, but it is difficult to interpret the inner shell pressure variations, that are neither expected in Sedov models nor in standard reverse shock models, unless the inner shell derives from projection effects.

We extract the spectra in four regions (P1,P2,P3,P4, see Fig. 1a) along the double shell following the energy variations (Fig. 1b). Since there are no soft emission structures as in the V-shaped region, we expect the plasma to consist mostly of shocked ISM and to be fitted by a single NEI thermal model. In most cases, the fits are slightly worse than a two component

EI model, except on the inner shell (Field P3), where the NEI fitting is bad ($\chi^2 \simeq 2.4$ instead of 1.1). With abundances of oxygen and iron lower than solar, the fits become acceptable. Table 4 summarizes the parameters of this model.

Only the variation of temperature is correctly constrained and shows two peaks in temperature. The uncertainties in the ionization parameter $n_e t$, abundances and N_H profiles are too large to quantify any possible gradient on these quantities. We note however that the suggested underabundance of iron and slight increasing gradient toward the interior is consistent with the expected depletion rates and with the fact that grains are destroyed by thermal sputtering on a time scale comparable to that of ionization relaxation in the gas (Itoh 1989). The spectral resolution of the PSPC renders difficult the abundance determination, but similar underabundances are found with the *ASCA* SIS (Decourchelle et al. 1996).

4. Discussion

The spectral analysis has shown that, in the soft regions, two temperatures are required, both for EI and NEI models. In the hot and tenuous regions, an acceptable solution is obtained with two temperatures although a single NEI model can account for the spectrum provided a lower column density ($N_H = 1. \pm 0.2 \cdot 10^{20} \text{ cm}^{-2}$) is allowed. Figs. 7a and 7b present the contribution of the soft and hot components of the A and B Field spectra for the best fit models. For EI models, the spectrum is dominated by the low temperature component whereas the contribution by the hot component is minor but essential for high energies. For NEI models the contribution of the components is modified : the hot component flux is enhanced whereas the soft component one is reduced in the PSPC band, as is illustrated on Figs. 7a and 7b. This leads to an incorrect estimate of the temperature and mass of the components if equilibrium ionization is assumed.

As a matter of fact, the value of the column density is not well known. HI observations at 21 cm (DeNoyer 1975) lead to a total column density in the line of sight to the Cygnus Loop of $1.5 - 3. \cdot 10^{21} \text{ cm}^{-2}$. A value of $7. - 15. \cdot 10^{20} \text{ cm}^{-2}$ toward the Cygnus Loop is suggested by the galactic HI distribution. From single EI models applied to Cygnus Loop X-ray spectra, the usual value of $4. \cdot 10^{20} \text{ cm}^{-2}$ is derived. But due to the non-orthogonality between the N_H and the low temperature in the fitting procedure, this determination is rather sensitive to the assumed model and to the energy band covered by the measurements. In the PSPC as well as in the *EXOSAT* (Ballet and Rothenflug 1989) energy bands, single temperature models result in an N_H value lower ($\simeq 10^{20} \text{ cm}^{-2}$) than that obtained with two component models (Tables 1 and 2). To derive precisely the column density in SNRs from X-ray data, we need a good spectral model over a wide energy band as well as good spectral resolution at low energies.

If we do not accept a lower value of N_H in the hot regions, there is no evident way to avoid two temperature models. The hot component comes most probably from the tenuous medium shocked by the blast wave, which is supported by the harder spectra seen in the inner diffuse region of the Cygnus Loop, as well as by the emission above 1 keV in softer region (bright

structures and shock front). We thus expect to see it in all spectra. The soft component is clearly associated with the bright emission structures (as along the V-shaped structure), indicating that the blast wave is interacting with clouds. Another signature is the emission of coronal lines (Fe X and Fe XIV), associated with the suggested clouds (Ballet et al. 1984, Teske and Kirshner 1985, Hester and Cox 1986, Ballet et al. 1989). They follow very well the soft emission along the V-shaped structure (Sauvageot and Decourchelle 1995). We thus would expect a confined soft component around the bright emission structures. For a conventional value of N_H , we also need this soft emission in faint diffuse region (as in Field B), or at the shock, where any indication of an interaction of the blast wave with clouds is absent. It would thus be very tempting to associate the soft component with interacting matter, even in places where the X-ray emission is diffuse, implying the presence of small clouds rather uniformly distributed. The idea of cloudlets was proposed by Cowie and McKee (1975) and by Fesen et al. (1982) to explain optical spectrophotometric data of the Cygnus Loop.

From the spectral analysis, we derive the densities of each component for each model. In Field A, we obtain roughly $n_1 \simeq 6 \text{ cm}^{-3}$, $n_2 \simeq 0.14 \text{ cm}^{-3}$ and in Field B, $n_1 \simeq 0.7 \text{ cm}^{-3}$, $n_2 \simeq 0.08 \text{ cm}^{-3}$. The hot component density is lower in the inner Field B than in the outer Field A, which is expected by classical Sedov models. If the soft component in Field B is created by shocked clouds, they should have a size smaller than the spatial resolution of the PSPC ($\simeq 30''$), thus typically less than 0.1 pc. If we assume that the density of the soft component in Field A is representative for the clouds inside the Cygnus Loop, we can reconsider the value of the filling factor (10%) that we have introduced for Field B. The soft X-ray emitting matter would thus fill 0.1% of the volume, which corresponds to $\simeq 400$ clouds with a size of 0.1 pc for Field B. Since the density depends on the volume estimate and on the distance, this only gives an order of magnitude.

5. Conclusion

The excellent spatial resolution of the HRI as well as comparison with optical data give new insights on the morphology of the V-shaped structure in the North Cygnus Loop. The "filamentary" appearance of the west arm including its south-west extension visible in X-rays and the optical band strongly suggests that it is independent of the east arm, with which no clear optical emission is associated. This view is supported by velocity measurements of iron coronal lines, which show that the V-shaped structure is likely to be due to geometrical projection effects (Sauvageot and Decourchelle 1995). The bow shock interpretation is thus definitively ruled out. Comparison between PSPC and optical data shows that nonradiative filaments are marking the north shock front. A striking optical filament is lying 20 arcmin inside the remnant (in projection) coinciding with the X-ray inner shell of the double structure.

The PSPC data put into evidence that the bright emission structures exhibit soft spectra, which we relate to shocked clouds, whereas the diffuse hot medium, located in the inner

Table 4. NEI model with free abundances of oxygen and iron along the double shell structure.

Fields	kT	$\log(n_e t)$	O	Fe	N_H	χ_r^2
	keV	$s\text{ cm}^{-3}$	Ab_{\odot}	Ab_{\odot}	cm^{-2}	
P1	0.31 ± 0.05	$10.5^{+0.45}_{-0.25}$	$0.77^{+0.1}_{-0.15}$	$0.4^{+0.5}_{-0.2}$	20.45 ± 0.15	0.84
P2	0.45 ± 0.06	10.3 ± 0.2	0.75 ± 0.1	$0.7^{+0.4}_{-0.3}$	20.4 ± 0.15	1.1
P3	0.38 ± 0.04	$10.3^{+0.22}_{-0.15}$	$0.4^{+0.1}_{-0.07}$	$0.8^{+0.5}_{-0.3}$	20.35 ± 0.15	1.2
P4	0.48 ± 0.1	10.25 ± 0.25	0.7 ± 0.1	$0.8^{+1.}_{-0.3}$	20.35 ± 0.2	1.2

* χ_r^2 is the reduced chi-squared value. The error bars are for the 90 % confidence level.

part of the remnant presents a higher temperature component. We have done a detailed spectral analysis of two very different fields (in morphology and spectrum). At low spectral resolution, we cannot distinguish between a two-temperature model with and without NEI effects, but we note that neglecting these NEI effects leads to an incorrect estimate of the temperature and mass of the components. Analysis of these spectra reveals that a bimodal temperature distribution is required in bright soft regions to model the data. The lower temperature gas may produce the observed O VI emission. The existence of large clouds ($\simeq 5$ pc), as observed in HI, can in a qualitative way explain the overall emission in X-rays, coronal lines and the optical band.

In the inner hot and tenuous region, a single NEI model with a rather low column density is sufficient to fit the data. However, in order to have a more standard value of N_H , we have to invoke a soft component in the X-ray spectra, which can be attributed to the emission from small cloudlets unresolved with the HRI.

Due to the large variations in the spectrum from place to place even at small scales, we need spectral-imaging data with a good energy resolution. The combined analysis of both *ROSAT* and *ASCA* data will help us to measure the abundances of the elements and to determine the scale of any NEI effects.

Acknowledgements. We wish to thank Monique Arnaud for many useful discussions and for providing us with the spectral codes. We also thank the referee John Raymond for his useful comments and for providing the O VI emissivities. We also thank Jeonghee Rho for a careful reading of the manuscript. A.D. and J.L.S. are grateful to MPE for its hospitality during their stay and to Osaka University where this paper was finalized. Part of this work used the EXSAS package.

References

Arendt R.G., Dwek E., Leisawitz D., 1992, ApJ 400, 562
 Arnaud M., Raymond J., 1992, ApJ 398, 394
 Arnaud M., Rothenflug R., 1985, A&AS 60, 425
 Aschenbach B., 1988, Appl. Opt., 27, No. 8, 1404
 Aschenbach B., 1992, in 'International Space Year' Conference on 'Space Sciences with particular emphasis on High-Energy Astrophysics', Eds. T.D. Guyenne and J.J. Hunt, ESA ISY-3, 41.
 Ballet J., Arnaud M., Rothenflug R., 1984, A&A 133, 357
 Ballet J., Caplan J., Rothenflug R., Dubreuil D., Soutoul A., 1989, A&A 211, 217
 Ballet J., Rothenflug R., 1989, A&A 218, 277
 Blair W.P., Long K.S., Vancura O., Holberg J.B., 1991, ApJ 374, 202
 Braun R., Strom R.G., 1986, A&A 164, 208
 Charles P.A., Kahn S.M., McKee C.F., 1985, ApJ 295, 456

Cowie L.L., McKee C.F., 1977, ApJ 211, 135
 Decourchelle A., Sauvageot J.L., Tsunemi H., Ballet J., 1996, in proceedings of "X-ray imaging and spectroscopy of cosmic hot plasmas", Ed. F. Makino, in press.
 DeNoyer L.K., 1975, ApJ 196, 479
 Graham J.R., Levenson N.A., Hester J.J., Raymond J.C., Petre R., 1995, ApJ 444, 787
 Green D.A., 1984, M.N.R.A.S. 211, 433
 Greidanus H., Strom R.G., 1992, A&A 257, 265
 Hester J.J., 1987, ApJ 314, 187
 Hester J.J., Raymond J.C., Danielson G.E., 1986, ApJL 303, L17
 Hester J.J., Cox D.P., 1986, ApJ 300, 675
 Hester J.J., Raymond J.C., Blair W.P., 1994, ApJ 420, 721
 Itoh H., 1989, PASJ 41, 853
 Jenkins E.B., Savage B.D., 1974, ApJ 187, 243
 Ku W.H.M., Kahn S.M., Pisarski R., Long K.S., 1984, ApJ 278, 615
 Kulkarni S.R., Hester J.J., 1988, Nature, 335, 801
 Mewe R., Gronenschild E.H.B.M., Van den Oord H.J., 1985, A&AS 62, 197
 Mewe R., Lemen J.R., Van den Oord H.J., 1986, A&AS 65, 511
 Meyer J.P., 1985, ApJS 57, 173
 Miyata E., Tsunemi H., Pisarski R., Kissel S.E., 1994, PASJ 46, L101
 Miyata E., Tsunemi H., Canizares C.R., 1995, ApJ submitted
 Minkowski R., 1958, Rev. Mod. Phys. 30, 1048
 Pfeiffermann E., Briel U.G., Hippmann H., Ketterring G., Metzner G., Predehl P., Reger G., Stephan K.-H., Zombeck M.V., Chappell J., Murray S.S., 1986, Proc. SPIE 733, 519
 Raymond J.C., 1991, PASP 103, 666
 Raymond J.C., Smith B., 1996, private communication
 Sauvageot J.L., Decourchelle A., 1995, A&A 296, 201
 Savage B.D., Mathis J.S., 1979, ARA&A 17, 73
 Seaton M.J., 1979, MNRAS 187, 73P
 Shull P.J., Dyson J.E., Kahn F.D., West K.A., 1985, MNRAS 212, 799
 Shull P.J., Hippelein H., 1991, ApJ 383, 714
 Teske R.G., Kirshner R.P., 1985, ApJ 292, 22
 Trümper J., 1983, Adv. Space Res., 2, No. 4, 241
 Tsunemi H., Manabe M., Yamashita K., Koyama K., 1988, PASJ 40, 449
 Vancura O., Raymond J.C., Dwek E., Blair W.P., Long K.S., Foster S., 1994, ApJ 431, 188
 Vedder P.W., Canizares C.R., Markert T.H., Pradhan A.K., 1986, ApJ 307, 269
 Woodgate B.E., Kirshner R.P., Balon R.J., 1977, ApJ 218, L129